

# Robust EMRAN based Neural Aided Learning Controller for Autonomous Vehicles

Sauranil Debarshi, Suresh Sundaram, and Narasimhan Sundararajan

**Abstract**—This paper presents an online evolving neural network-based inverse dynamics learning controller for an autonomous vehicle's longitudinal and lateral control under model uncertainties and disturbances. The inverse dynamics of the vehicle are approximated using a feedback error learning mechanism that utilizes a dynamic Radial Basis Function neural network, referred to as the Extended Minimal Resource Allocating Network (EMRAN). EMRAN uses an extended Kalman filter approach for learning and a growing/pruning condition helps in keeping the number of hidden neurons minimum. The online learning algorithm helps in handling the uncertainties and dynamic variations and also the unknown disturbances on the road. The proposed control architecture employs two coupled conventional controllers aided by the EMRAN inverse dynamics controller. The control architecture has a conventional PID controller for longitudinal cruise control and a Stanley controller for lateral path-tracking. Performances of both the longitudinal and lateral controllers are compared with existing control methods and the simulation results clearly indicate that the proposed control scheme handles the disturbances and parametric uncertainties better, and also provides better tracking performance in autonomous vehicles.

**Index Terms**—Autonomous vehicles, cruise control, path-tracking, adaptive control, EMRAN.

## I. INTRODUCTION

RECENT advancements in Advanced Driver Assistance Systems (ADAS) have opened the doors for numerous prototypes of autonomous vehicles (AVs) to operate on our roads and streets. The main objectives here have been to ensure guaranteed performance, enhanced safety, and increased efficiency while maintaining passenger comforts. These require a collective operation of various aspects of vehicle autonomy, such as perception, planning, control, and situational awareness [1]. One inherent feature needed in these AVs is to provide control signals to the actuators, enabling navigation through complex, unstructured environments without any human intervention.

Longitudinal control of AVs involves controlling the brake and throttle [2], with applications in Adaptive Cruise Control (ACC) [3], emergency brake assist system [4], and velocity tracking [5]. With the emergence of vehicle-to-vehicle (V2V) communication, the next generation of longitudinal control systems need cooperative adaptive cruise control schemes [6], [7]. Cooperative ACC improves the current intelligent transportation system (ITS) involving enhanced safety, mobility, and sustainability [8].

Sauranil Debarshi and Suresh Sundaram are with the Department of Aerospace Engineering, Indian Institute of Science, Bangalore, India. (email: sauranild@iisc.ac.in, vssuresh@iisc.ac.in)

Narasimhan Sundararajan is with the School of Electrical and Electronics Engineering, Nanyang Technological University, Singapore. (email: ensundara@ntu.edu.sg)

A great deal of research efforts has been carried out in using learning-based methods for longitudinal control of AVs [9], [10], [11]. A neuro-fuzzy system that incorporates both the ride comfort and safety was demonstrated in [12] to keep the vehicle at a target speed. In [13], the authors proposed a reinforcement learning controller that predicts the future speed reference values and disturbances. Many works can be found in the literature on adaptive neural networks to control the longitudinal dynamics of AVs [14], [15]. These controllers, with their online adaptive capabilities, provide robustness against parametric uncertainties and disturbances.

In autonomous driving, lateral control methods involve steering a vehicle along the desired trajectory without losing its stability [16], [17], [18]. In [19], the authors demonstrated a three-phase automatic overtaking maneuver using an adaptive nonlinear controller that estimates the velocity of the overtaking vehicle. A backstepping variable structure control (BVSC) coupled to a RBF neural network (RBFNN) was presented in [20]. The BVSC steers the vehicle, while the RBFNN acts as the estimator for the nonlinearities arising from tire uncertainties. It eliminates path-tracking errors, and maintains the yaw stability of the vehicle. In another study, a type-2 fuzzy neural PID controller was employed to minimize the heading and lateral errors during a double lane change maneuver [21]. Additionally, they had presented an adaptive neural network-based Extended Kalman Filter (EKF) to eliminate the effects of external disturbances and parametric uncertainties. A control method based on a neural network PID control was presented in [22]. Lateral  $H_\infty$  motion controllers have been described in [23], [24]. Other control schemes have also been used, such as a linear quadratic regulator (LQR) [25] and a sliding mode controller [26], [27]. Moreover, emphasis on yaw stability while designing the lateral controllers is indispensable since harsh, undesirable motions may cause the vehicle to spin, drift, and become unstable. Several control algorithms utilizing fuzzy logic control [28], model predictive control [29], [30], and adaptive neural control using a random projection neural network (RPNN) [31] have been proposed in the literature to improve both vehicle handling and safety.

Adaptive neural networks (ANNs) with their ability to approximate unknown nonlinear functions have also been widely used for various control applications [32], [33]. The EMRAN inverse dynamics controller is one such example of ANNs. Many works related to EMRAN for both aircraft and structural control applications have been presented in the literature. Pashilkar *et al.* [34] designed a fault-tolerant auto-landing controller for an aircraft using a feedback error learning approach. The robustness of the EMRAN controller was

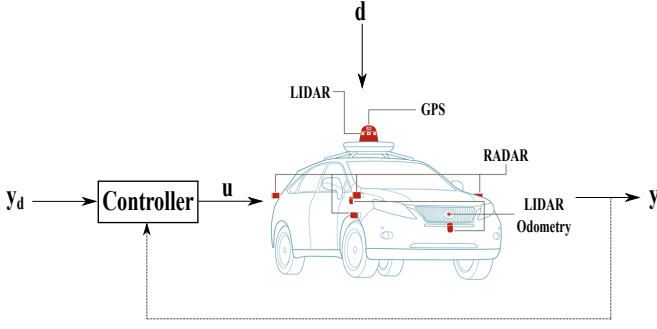


Fig. 1. Schematic representation of a typical vehicle control architecture.

verified against actuator failures during landing. Fault-tolerant control of nonlinear base-isolated structural models during earthquakes were presented in [35], [36]. In [37], an engine vibration controller was discussed. In all of these works, the EMRAN controller has proven to be an effective algorithm in providing good control performance in the presence of unwanted nonlinearities and uncertainties.

In this paper, we use a sequential learning Radial Basis Function (RBF) neural network *i.e.*, the Extended Minimal Resource Allocation Network (EMRAN) [38] to present two coupled neuro-aided control schemes, the first one for longitudinal cruise control and the second for lateral path-tracking in AVs. EMRAN is an online adaptive, model-free neural network that approximates the inverse dynamics of the vehicle using a feedback error learning strategy. It acts as an aid to the conventional controllers (PID and Stanley) by providing robustness against various disturbances and uncertainties. Furthermore, the proposed neuro-controllers are computationally inexpensive because of the growing/pruning strategy employed by the EMRAN network. The performance of both the longitudinal and lateral inverse dynamics learning controllers is investigated individually (decoupled) and in a coupled state. It is assumed that the lateral dynamics of the vehicle do not affect the longitudinal controller, and vice versa, in the decoupled phase. In the coupled state, we integrate both the controllers without any assumptions so as to simulate the dynamics of an actual vehicle. We test the EMRAN-based path-tracking controller by keeping the velocity of the AV constant with the proposed longitudinal controller. Their performances are also evaluated against classical feedback methods and other disturbance rejection schemes.

Rest of the paper is organized as follows. In Section II, the problem statement related to AV control is formulated. Section III discusses the EMRAN based inverse dynamics learning controller. Performance evaluation using simulation results is shown in Section IV. Finally, the conclusions based on the study are summarized in Section V.

## II. PROBLEM FORMULATION

Before presenting the mathematical model of the nonlinear vehicle, we first formulate the control problem in AVs to track a reference signal  $\mathbf{y}_d$ . As shown in Fig. 1, an AV requires multiple onboard sensors to replicate the human understand-

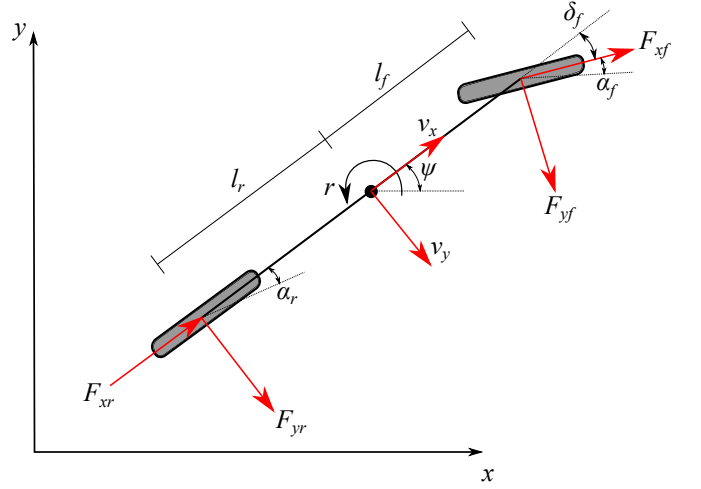


Fig. 2. Nonlinear single-track vehicle dynamics model.

ing of its location, perception, and navigation. The sensors provide critical information to the controller for generating control inputs such that the vehicle can track the reference signals with minimum errors. This paper investigates the AVs' longitudinal and lateral control problem through cruise control and Double Lane Change (DLC) maneuvers. The state-space representation of the vehicle is considered as:

$$\dot{\mathbf{x}} = g(\mathbf{x}, \mathbf{u}_v, t) \quad (1)$$

where  $\mathbf{u}_v$  is the  $q$ -dimensional control inputs and  $\mathbf{x}$  is the  $m$ -dimensional state vector. The control vector ( $\mathbf{u}_v$ ) belongs to a class of permissible inputs:

$$U := \{\mathbf{u}_v : \|\mathbf{u}_v(t)\| \leq \zeta, t > t_0\} \quad (2)$$

where  $\zeta$  is a real positive number.

With the constrained control input ( $\mathbf{u}_v$ ), we define the control objective such that the vehicle's output follows the reference signal accurately, *i.e.*,

$$\|\mathbf{y}_d - \mathbf{y}\| \rightarrow 0 \quad (3)$$

where  $\mathbf{y}$  is the output vector of the vehicle.

The AV considered in this study is a nonlinear single-track or "bicycle model", as depicted in Fig. 2. The dynamics of the bicycle model can be described as [39], [40]:

$$\begin{cases} \dot{x} = v_x \cos \psi - v_y \sin \psi \\ \dot{y} = v_x \sin \psi + v_y \cos \psi \\ \dot{\psi} = r \\ \dot{v}_x = \frac{1}{m}(F_{xf} + F_{xr}) + v_y r \\ \dot{v}_y = \frac{1}{m}(F_{yf} + F_{yr}) - v_x r \\ \dot{r} = \frac{1}{I_z}(F_{yf} l_f - F_{yr} l_r) \\ \omega_{wf} = \frac{1}{I_w}(T_d - R_t F_{xf} - T_b) \\ \omega_{wr} = \frac{1}{I_w}(T_d - R_t F_{xr} - T_b) \end{cases} \quad (4)$$

where,

- $x$ : longitudinal displacement in global frame;
- $\dot{x}$ : longitudinal velocity in global frame;
- $y$ : lateral displacement in global frame;
- $\dot{y}$ : lateral velocity in global frame;
- $v_x$ : longitudinal velocity in vehicle frame;
- $v_y$ : lateral velocity in vehicle frame;
- $\psi$ : yaw angle;
- $r$ : vehicle yaw rate;
- $w_{wf}$ : angular velocity of the front wheel;
- $w_{wr}$ : angular velocity of the rear wheel;
- $F_{xf}$ : longitudinal tire force of the front wheel;
- $F_{xr}$ : longitudinal tire force of the rear wheel;
- $F_{yf}$ : lateral tire force of the front wheel;
- $F_{yr}$ : lateral tire force of the rear wheel;
- $T_d$ : driving torque;
- $T_b$ : brake torque;
- $m$ : vehicle mass;
- $R_t$ : static wheel radius;
- $I_z$ : yaw moment of inertia;
- $I_w$ : moment of inertia of the wheel

For the tire force terms in Eq. (4), an analytical tire model developed by Salaani [41] has been used to estimate the longitudinal and lateral forces. This nonlinear tire model captures the wheel-road dynamics accurately and has been validated from experimental data using four different tires. The longitudinal and lateral wheel forces are given as:

$$\begin{cases} F_{xi} = -\frac{\kappa_i F_{zi} C_{\kappa i} f_{ai}(\sigma)}{\sqrt{\left(\frac{C_{\kappa i} \kappa_i}{\mu_{pxi}}\right)^2 + \left(\frac{C_{\alpha i} \tan(\alpha_i)}{\mu_{pyi}}\right)^2}} \\ -\frac{\kappa_i F_{zi} C_{\kappa si} f_{si}(\sigma)}{\sqrt{\left(\frac{C_{\kappa si} \kappa_i}{\mu_{sxi}}\right)^2 + \left(\frac{C_{\alpha i} \tan(\alpha_i)}{\mu_{syi}}\right)^2}} \\ F_{yi} = \frac{C_{\alpha i} \tan(\alpha_i) F_{zi} f_{ai}(\sigma)}{\sqrt{\left(\frac{C_{\kappa i} \kappa_i}{\mu_{pxi}}\right)^2 + \left(\frac{C_{\alpha i} \tan(\alpha_i)}{\mu_{pyi}}\right)^2}} \\ + \frac{C_{\alpha i} \tan(\alpha_i) F_{zi} f_{si}(\sigma)}{\sqrt{\left(\frac{C_{\kappa si} \kappa_i}{\mu_{sxi}}\right)^2 + \left(\frac{C_{\alpha i} \tan(\alpha_i)}{\mu_{syi}}\right)^2}} \end{cases} \quad (i = f, r) \quad (5)$$

where  $F_{zi}$ ,  $\kappa_i$ , and  $\alpha_i$  are the wheel load, longitudinal slip ratio, and slip angle, respectively.  $C_{\kappa i}$  and  $C_{\alpha i}$  denote the longitudinal and lateral tire stiffness, while  $C_{\kappa si}$  represents the longitudinal stiffness in sliding mode. The peak/sliding coefficients of friction in the longitudinal and lateral directions are given by  $\mu_{pxi}$ ,  $\mu_{sxi}$ ,  $\mu_{pyi}$ , and  $\mu_{syi}$ , where the subscript  $i$  denotes the front and rear tires.

Using small angle approximations, the tire slip angle in the front ( $\alpha_f$ ) and rear ( $\alpha_r$ ) can be linearized as [42]:

$$\begin{cases} \alpha_f = \arctan\left(\frac{\dot{y} + l_f \dot{\psi}}{\dot{x}}\right) - \delta_f \approx \frac{\dot{y} + l_f \dot{\psi}}{\dot{x}} - \delta_f \\ \alpha_r = \arctan\left(\frac{\dot{y} - l_r \dot{\psi}}{\dot{x}}\right) \approx \frac{\dot{y} - l_r \dot{\psi}}{\dot{x}} \end{cases} \quad (6)$$

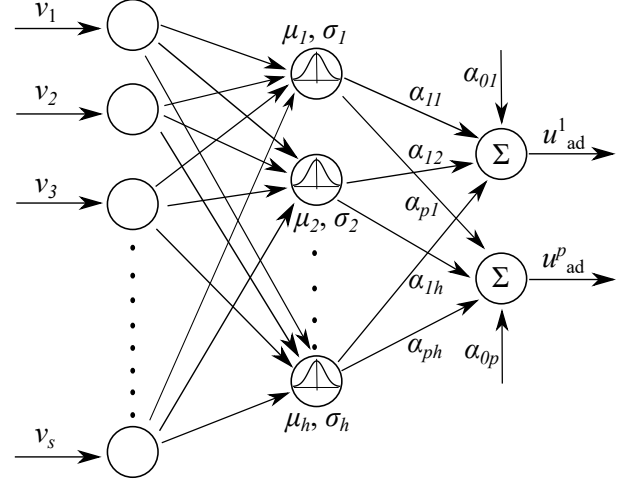


Fig. 3. EMRAN architecture with Gaussian activation functions.

where  $l_f$  and  $l_r$  are, respectively, the distances to the front and rear axles from the center of gravity (CoG) of the vehicle. The steering angle is represented by  $\delta_f$ . Additionally, the tire slip ratio ( $\kappa_i$ ) is defined as [43]:

$$\kappa_i = \frac{R_{ei} \omega_{wi} - v_x}{\max(R_{ei} \omega_{wi}, v_x, \epsilon)} \quad (i = f, r) \quad (7)$$

where  $R_{ei}$  is the effective tire radius and  $\omega_{wi}$  is the wheel angular velocity.  $\epsilon$  is a small constant ( $\epsilon \ll 1$ ) to avoid zero denominator.

With the control objective in Eq. (3) and the vehicle dynamics model in Eq. (4), the EMRAN aided online inverse dynamics learning controller is described in the following section.

### III. INVERSE DYNAMICS LEARNING EMRAN CONTROLLER

This section describes the EMRAN-based inverse dynamics learning control for improving the tracking performance of AVs. Before describing the controller architecture and functioning, a brief review of the working of EMRAN is presented next.

#### A. Extended Minimal Resource Allocating Network (EMRAN)

EMRAN is a fast, online learning algorithm developed by Li *et al.* [38]. It implements a compact RBF neural network by incorporating a fully adaptive learning strategy, with the capability to add and prune the hidden neurons based on the network inputs and the responses of the controlled object.

As shown in Fig. 3, the EMRAN architecture consists of a single hidden layer with zero hidden neurons initially. The coefficients  $\alpha_{jk}$  are the interconnection weights between the hidden and the output layer. The activation functions used in the hidden layer are Gaussian, whose outputs are given by:

$$z^k = \exp\left(\frac{-\|\mathbf{v} - \boldsymbol{\mu}_k\|^2}{2(\sigma_k)^2}\right) \quad (8)$$

where  $\mathbf{v}$  is the  $s$ -dimensional network input, while  $\boldsymbol{\mu}_k$  and  $\sigma_k$  are the center and width of a typical hidden neuron  $k$ , respectively. The outputs of the neural network are then given by:

$$w_{ad}^j = \sum_{k=1}^h \alpha_{jk} z^k + \alpha_{0j} \quad (j = 1, 2, \dots, p) \quad (9)$$

where  $\alpha_{0j}$  are the biases at the output layer and  $j$  is the total outputs of the network.

EMRAN starts with no hidden neurons. A new neuron is added when the following criteria are satisfied at any time step,  $\tau$ :

$$\begin{cases} \|\mathbf{v}[\tau] - \boldsymbol{\mu}_w[\tau]\| > \epsilon_1[\tau] \\ \|\mathbf{y}_e[\tau]\|^2 \geq \epsilon_2 \\ J_{rmse} = \sqrt{\frac{\sum_{\tau=l-S_w+1}^l \|\mathbf{y}_e[\tau]\|^2}{S_w}} \geq \epsilon_3 \end{cases} \quad (10)$$

where  $\epsilon_1[\tau] = \max[\epsilon_{max}\gamma^{\tau-1}, \epsilon_{min}]$ ,  $\gamma$  is a decay constant and represents the scale of resolution [44],  $\boldsymbol{\mu}_w$  is the center of the hidden neuron closest to  $\mathbf{v}[\tau]$ . This neuron constitutes the ‘winner neuron.’  $S_w$  is the sliding window’s length and  $\epsilon_1$ ,  $\epsilon_2$ , and  $\epsilon_3$  are the thresholds. The distance between the new observation and all the existing nodes is compared by the first criterion. The second criterion ascertains that the existing neurons are sufficient to produce a reasonable network output. The third criterion is based on the root mean square error for the window of samples  $S_w$ , which controls the noise from over-fitting the neurons. The parameters of the newly added hidden neuron are given by:

$$\begin{cases} \boldsymbol{\alpha}_{k+1}[\tau] = \mathbf{y}_e[\tau - 1] \\ \boldsymbol{\mu}_{k+1}[\tau] = \mathbf{v}[\tau] \\ \sigma_{k+1}[\tau] = \kappa \|\mathbf{v}[\tau] - \boldsymbol{\mu}_w[\tau]\| \end{cases} \quad (11)$$

where  $\kappa$  determines the overlap of the responses of the hidden neurons in the input space. When the criteria are not satisfied, an Extended Kalman Filter (EKF) updates the network parameters, namely the connection weights, biases, centers, and widths of the network based on the values from the previous time step. To achieve faster learning for online applications, only the parameters of the winner neuron are updated as follows:

$$\mathbf{NP}^w[\tau] = \mathbf{NP}^w[\tau - 1] + \mathbf{K}^w[\tau] \|\mathbf{y}_e[\tau - 1]\| \quad (12)$$

where  $\mathbf{K}^w[\tau]$  is the Kalman gain matrix given by:

$$\mathbf{K}^w[\tau] = \mathbf{P}^w[\tau - 1] \mathbf{B}^w[\tau] (\mathbf{R}[\tau] + \mathbf{B}^w[\tau]^T \mathbf{P}^w[\tau - 1] \mathbf{B}^w[\tau])^{-1} \quad (13)$$

where  $\mathbf{B}^w[\tau] = \nabla_{\mathbf{w}} \mathbf{u}_{ad}$  is the gradient matrix of  $\mathbf{u}_{ad}$  with respect to the parameter vector  $\mathbf{w}[\tau]$  evaluated at  $\mathbf{w}[\tau - 1]$ .  $\mathbf{R}[\tau]$  is the variance of the measurement noise and  $\mathbf{P}^w[\tau]$  is the error of the covariance matrix, which is updated by:

$$\mathbf{P}^w[\tau] = (\mathbf{I} - \mathbf{K}^w[\tau] \mathbf{B}^w[\tau]^T) \mathbf{P}^w[\tau - 1] + q \mathbf{I} \quad (14)$$

where  $q$  is a scalar quantity that determines the allowed random step in the direction of the gradient vector. When a

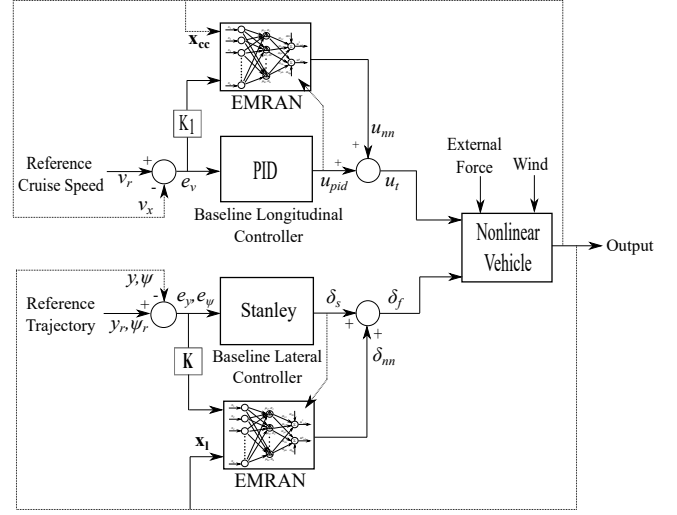


Fig. 4. Schematic of the proposed EMRAN aided control architecture.

new hidden unit is added to the network, the dimensionality of the covariance matrix increases to:

$$\mathbf{P}^w[\tau] = \begin{bmatrix} \mathbf{P}^w[\tau - 1] & 0 \\ 0 & P_0 \mathbf{I} \end{bmatrix} \quad (15)$$

where  $P_0$  is a scalar value that represents the uncertainty in the initial parameters of the new hidden neuron.

EMRAN incorporates a pruning strategy for maintaining a compact network by ensuring that the neurons that have not been contributing significantly (based on a threshold parameter ( $\delta$ ) to the network performance for a predefined period of time ( $N_w$ ), are pruned from the network. It results in a network that is computationally inexpensive and adapted to fast real-time online applications. Moreover, since only the parameters of the winner neuron are updated, the computations required to update its parameters is  $O(l^3)$ , where  $l$  is the number of parameters of the nearest neuron. Therefore, the total computational burden at each step is  $8^3$  floating point operations (FLOPS) ( $1 \text{ FLOP} = 1e^{-06} \text{ s}$ ), which is relatively small. Control output calculation is  $O(h)$ , where  $h$  is the number of hidden neurons. Next, the EMRAN aided control architecture and its functioning for AV control are described.

#### B. EMRAN based Inverse Vehicle Dynamics Learning

Consider the dynamics of the vehicle in Eq. (4) to be in the form of:

$$\dot{\mathbf{x}} = g(\mathbf{x}, \mathbf{u}_v) \quad (16)$$

where  $\mathbf{u}_v = [u_t, \delta_f]$  constitutes the longitudinal and lateral control inputs to the AV. In this paper, we utilize the feedback error learning technique of Gomi *et al.* [45] to learn the inverse dynamics of the vehicle using the EMRAN neural network. By learning the inverse dynamics, EMRAN can compensate for the nonlinearities of the vehicle such that it follows the desired response set closely. The inversion can be represented by the equation:

$$\mathbf{u}_v = g^{-1}(\dot{\mathbf{x}}, \mathbf{x}) \quad (17)$$

Further, if the function  $g^{-1}$  is changing with time due to external factors, the neural controllers can generate immediate corrective actions to compensate for such changes. The architecture of the EMRAN aided controller is shown in Fig. 4.

From Fig. 4, it may be noted that both the longitudinal and lateral control inputs to the AV are the sums of the respective EMRAN network output and the baseline controller output, *i.e.*,

$$\begin{cases} u_t = u_{pid} + u_{nn} \\ \delta_f = \delta_s + \delta_{nn} \end{cases} \quad (18)$$

The output vectors of the baseline controllers and the online neural network are defined as  $\mathbf{u}_b = [u_{pid}, \delta_s]$  and  $\mathbf{u}_{nn} = [u_{nn}, \delta_{nn}]$ , respectively. In this controller scheme, the baseline controllers provide the basic stability requirements and generate the signals to train the EMRAN networks online. The neural network compensates for the disturbances and parametric uncertainties of the vehicle, thus aiding the baseline controllers in order to achieve a better tracking performance.

### C. Baseline Controller Design

The inner loop of the longitudinal cruise control uses a fully tuned PID controller as the baseline controller. It generates acceleration and deceleration commands ( $u_{pid}$ ) based on the differences between the reference ( $v_r$ ) and actual ( $v_x$ ) velocities. The drive torque ( $T_d$ ) and brake torque ( $T_b$ ) are ultimately computed from the acceleration/deceleration commands using dynamic equations. The input vector ( $\mathbf{x}_{cc}$ ) to the cruise control EMRAN consists of the longitudinal states of the vehicle, namely the position ( $x$ ), velocity ( $v_x$ ), and acceleration ( $a_x$ ). The output of the PID controller ( $u_{pid} = u_t - u_{nn}$ ) is used as the signal for updating the weights and neurons of the network. EMRAN learns this signal over time and generates the inverse longitudinal dynamics of the vehicle. However, it may not achieve better results than the baseline controller if it learns only from the PID controller. Hence, to get better performance, the learning signal is modified by adding a scaled ( $K_1$ ) velocity error signal to the output of the PID controller.

Similarly, for the lateral path-tracking controller, a Stanley controller [46] is used in the inner loop. The Stanley controller is a geometrical path-tracking algorithm developed by the Stanford University's DARPA grand challenge team. It is a nonlinear feedback function of the cross-track/lateral ( $e_y$ ) and heading ( $e_\psi$ ) errors measured from the vehicle's front axle. The steering angle is given by:

$$\delta_s = e_\psi + \tan^{-1} \left( \frac{k_f e_y}{v_x} \right) \quad (19)$$

where  $k_f$  is the position gain in the forward motion, and  $v_x$  is the longitudinal velocity of the vehicle. Moreover, as it considers both the heading and the lateral errors, it has shown to perform well in previous studies [47], [48]. Similar to the longitudinal control architecture, the lateral states of the vehicle are given as inputs ( $\mathbf{x}_l$ ) to the path-tracking EMRAN. The output of the Stanley controller ( $\delta_s$ ) added to the scaled ( $\mathbf{K} = [K_2, K_3]$ ) error signal, is given as the excitation signal to

TABLE I  
VEHICLE PARAMETERS

Parameters	Values
$m$	1480 kg
$I_z$	2350 kg.m <sup>2</sup>
$l_f$	1.05 m
$l_r$	1.63 m
$C_f$	67500 N/rad
$C_r$	47500 N/rad

the EMRAN network for learning the inverse lateral dynamics of the vehicle.

## IV. SIMULATION RESULTS

In this section, the performances of the proposed EMRAN based controllers are evaluated in a typical autonomous vehicle performing cruise control and double lane change (DLC) maneuvers. Simulations have been conducted in Matlab/Simulink-UE4 interface for cases with and without external disturbances/uncertainties scenarios. The physical parameters of the vehicle used for the simulations study are given in Table I, where  $C_f$  and  $C_r$  are the stiffness values of the front and rear tires, respectively. Moreover, the hyperparameters ( $\epsilon_{max}$ ,  $\epsilon_{min}$ ,  $\gamma$ ,  $\epsilon_2$ ,  $\epsilon_3$ ,  $\delta$ ,  $N_w$ ,  $S_w$ ,  $\kappa$ ,  $P_0$ ,  $q$ , and  $r$ ) associated with EMRAN are problem-dependent and are determined offline through an optimization by a Genetic Algorithm (GA) for achieving the best results. Note that these hyperparameters remain constant throughout the simulations. The GA parameters used in finding the best EMRAN parameters are as follows: crossover probability of 0.8, selection probability of 0.08, mutation probability of 0.15, maximum number of generations of 10, and a population size of 20. For a detailed description of optimization using a genetic algorithm, refer to [49].

The parameters of both the longitudinal and lateral EMRAN controllers are optimized independently using GA by minimizing their respective fitness functions, which are the root-mean-square (RMS) errors between the reference and actual values. For optimizing the longitudinal EMRAN, the desired cruise speed of 15 m/s is set in the vehicle, and it is assumed that the vehicle moves on a straight road. The RMS error of the velocity is used as the objective function to be minimized by the GA. For the path-tracking EMRAN controller, a DLC maneuver at a constant longitudinal velocity of 10 m/s is

TABLE II  
GA OPTIMIZED LONGITUDINAL AND LATERAL EMRAN PARAMETERS

Parameters	Longitudinal	Lateral
$\epsilon_{max}$	7.455	4.003
$\epsilon_{min}$	3.938	3.086
$\gamma$	0.915	0.981
$\epsilon_2$	0.357	0.005
$\epsilon_3$	0.071	0.003
$\delta$	0.091	0.073
$N_w$	12	9
$S_w$	10	14
$\kappa$	0.609	0.603
$P_0$	1.079	1.155
$q$	0.015	0.001
$r$	1.074	1.120

TABLE III  
RMS AND MAXIMUM VALUES OF TRACKING ERRORS

Controller	$e_{v_{rms}}$	$e_{v_{max}}$
PID	0.0149 m/s	0.0784 m/s
PID-EMRAN	0.0017 m/s	0.0332 m/s

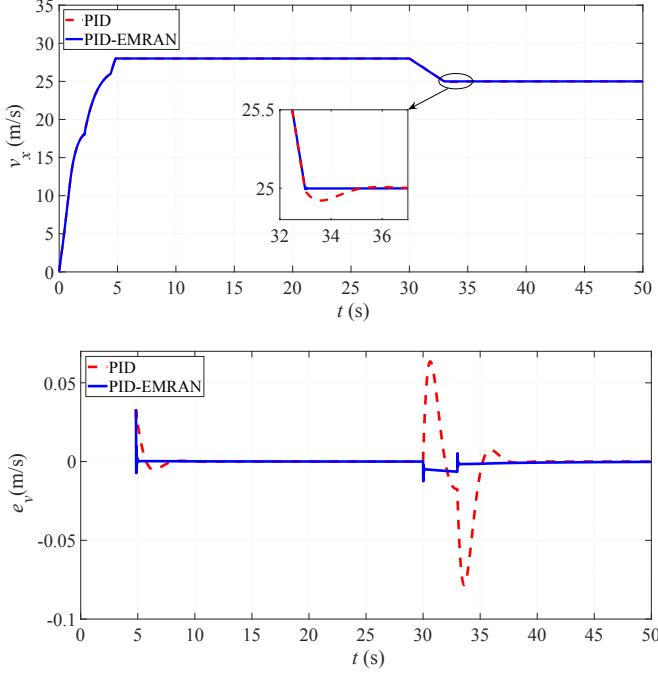


Fig. 5. Speed profile and error during a cruise speed change.

performed. The optimized parameters of both the controllers are given in Table II.

#### A. Longitudinal Cruise Control

1) *Case I: No Disturbance:* To evaluate the performance of the EMRAN aided PID controller (PID-EMRAN) at ideal conditions, the vehicle's cruising speed is changed from 28 m/s to 25 m/s at time  $t = 30$  s. Also, it is assumed that the vehicle travels on a dry asphalt ( $\mu = 1.0$ ), straight road. The proportional ( $K_P$ ), integral ( $K_I$ ), and derivative ( $K_D$ ) gains associated with the PID controller are set as 1.841, 2.603, and 0.682, respectively.

The performance of the baseline PID and neuro-aided PID-EMRAN controllers to track the reference cruise speed is shown in Fig. 5. The PID-EMRAN controller outperforms the PID-based approach by lowering the overshoots and undershoots. Table III validates this claim, which shows the RMS ( $e_{v_{rms}}$ ) and maximum ( $e_{v_{max}}$ ) values of the errors. Significant improvements are observed, with the PID-EMRAN controller reducing both the  $e_{v_{rms}}$  and  $e_{v_{max}}$  by 88.59% and 57.65% respectively. The neuron growth history in EMRAN is shown in Fig. 6. EMRAN controller adds hidden neurons to compensate for the errors during the change in cruise speed, thus tracking the reference signal more accurately during the transition.

2) *Case II: External Disturbances and Parametric Uncertainties:* In order to evaluate the disturbance rejection

TABLE IV  
ERROR CHARACTERISTICS IN PRESENCE OF DISTURBANCE

Controller	$e_{v_{rms}}$	$e_{v_{max}}$
PID	0.1368 m/s	0.5145 m/s
PID-EMRAN	0.0163 m/s	0.0817 m/s

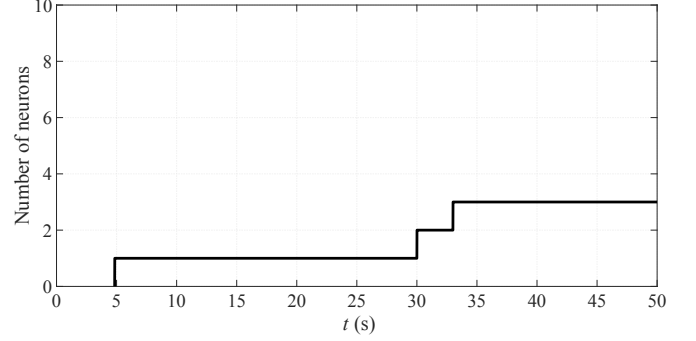


Fig. 6. Neuron history for tracking the cruise speed.

ability of the proposed longitudinal controller under extreme conditions, the vehicle was subjected to road inclinations of  $\pm 40^\circ$ . The vehicle starts on a level road initially ( $t < 10$  s) and encounters an uphill road with an inclination of  $40^\circ$  from  $t = 10$  s to  $t = 20$  s. At  $t = 20$  s, the slope reduces to zero, and the vehicle starts moving on the level road for another 10 seconds. Similar test cases were performed for the subsequent duration of the simulation, in which the vehicle started descending on a steep road of slope  $-40^\circ$  from  $t = 30$  s to  $t = 40$  s, after which it started moving on a level road again.

Figure 7 shows the performances of both the stand-alone

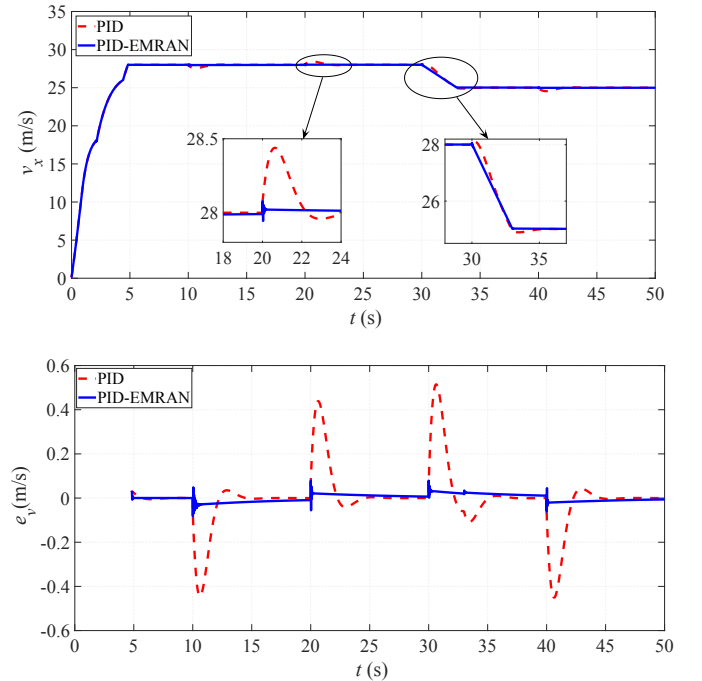


Fig. 7. Cruise speed profile and velocity error in presence of road inclinations.

TABLE V  
ERRORS IN THE PRESENCE OF PARAMETRIC UNCERTAINTIES

Controller	$e_{v_{rms}}$	$e_{v_{max}}$
PID	0.1463 m/s	0.2678 m/s
PID-EMRAN	0.0076 m/s	0.0340 m/s

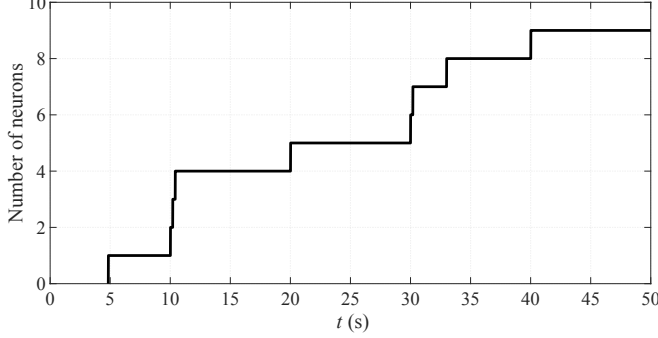


Fig. 8. Neuron history of longitudinal EMRAN for varying road inclinations.

PID and EMRAN-based PID controllers in the presence of the road disturbances. The proposed control architecture shows robustness against the varying road inclinations by minimizing the overshoot/undershoots and the steady-state errors. The vehicle also maintains smooth transitions in cruise speed. It has been verified quantitatively in Table IV by calculating the RMS and maximum errors. For this case, the PID-EMRAN improves the tracking errors by 86.88% ( $e_{v_{rms}}$ ) and 81.85% ( $e_{v_{max}}$ ). The neuron history is also shown in Fig. 8. It can be inferred by comparing Fig. 6 and Fig. 8 that the EMRAN controller constantly adds new neurons to mitigate the errors due to the disturbances, thus showing the effectiveness in its online learning ability. Because of the various instances of road inclinations during the simulation, no pruning of hidden neurons is observed.

Similarly, uncertainties related to vehicle parameters, ( $m = m + 0.15m \sin(t)$ ) and ( $I_y = I_y + 0.2I_y \sin(t)$ ) were included, where  $I_y$  is the pitch moment of inertia. Additionally, environmental perturbations of the road-friction coefficient ( $\mu = \mu + 0.5\mu \sin(t)$ ) and wind velocity ( $V_w = 15 * \sin(t)$ ) in the longitudinal direction were also considered.

Table V shows that even with the large parametric uncertainties and external perturbations, the proposed controller can track the reference cruise speed with minimum errors. The PID-EMRAN scheme clearly improves the speed tracking performance with or without disturbances/uncertainties, thereby improving vehicle safety in terms of minimizing the risk of collisions with nearby vehicles.

### B. Lateral Path-tracking Control

Double lane change (DLC) maneuvers at constant longitudinal velocities are performed to evaluate the performance of the proposed EMRAN aided Stanley (Stanley-EMRAN) controller. The reference trajectory in terms of lateral displacement

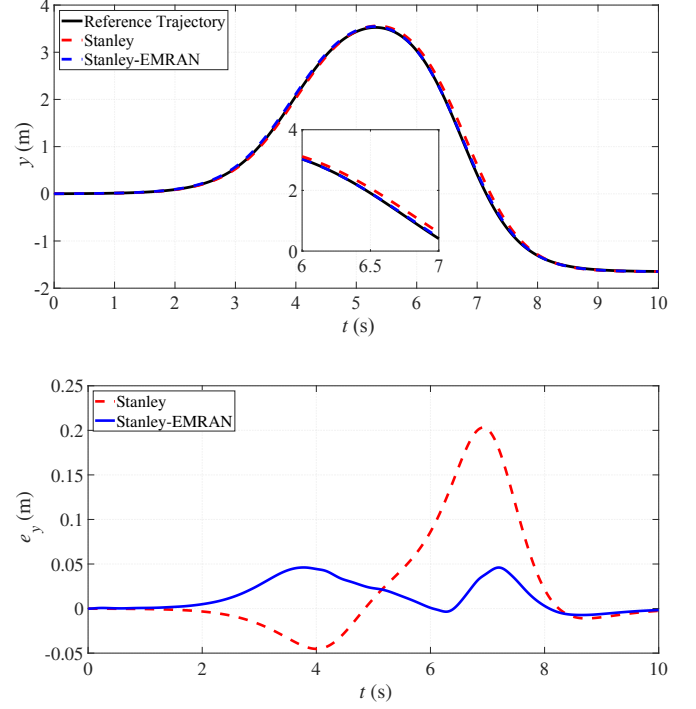


Fig. 9. Vehicle trajectory and corresponding lateral error without external disturbances.

( $y_r$ ) and yaw angle ( $\psi_r$ ) are expressed as in [18]:

$$\begin{cases} y_r = \frac{4.05}{2}(1 + \tanh(a)) - \frac{5.7}{2}(1 + \tanh(b)) \\ \psi_r = \arctan \left( 4.05 \left( \frac{1}{\cosh(a)} \right)^2 \left( \frac{1.2}{25} \right) - 5.7 \left( \frac{1}{\cosh(b)} \right)^2 \left( \frac{1.2}{21.95} \right) \right) \end{cases} \quad (20)$$

where  $a = \frac{2.4(v_x t - 27.19)}{25} - 1.2$  and  $b = \frac{2.4(v_x t - 56.46)}{21.95} - 1.2$ . The results of the proposed lateral controller with and without disturbances/uncertainties are presented next.

1) *Case I: Slow Speed and No Disturbance*: In this case, the vehicle performs the DLC at a constant velocity of 10 m/s and without any external disturbances. Figure 9 shows the lateral position ( $y$ ) and the corresponding lateral error ( $e_y$ ) for the baseline Stanley and Stanley-EMRAN controllers. Table VI presents a quantitative comparison of their performances in terms of the RMS and maximum values of the lateral and heading angle errors. The proposed neuro-controller improves the trajectory tracking by reducing the peak lateral offset ( $e_{y_{max}}$ ) by 77.25% during the DLC maneuver. The responsiveness of the vehicle to lane change has also improved compared to that of Stanley. Additionally, the vehicle's ability to follow the reference heading is achieved rapidly with a smaller maximum error (Fig. 10), which decreased by 42.72%. It is evident from the results that the proposed controller significantly improves the trajectory following ability of the vehicle. The reduced lateral error limits vehicle collision during sudden lane changes.

Also, a comparative analysis has been done with the recently developed EKF-based type-2 fuzzy neural network (EKF-



TABLE VI  
ERROR CHARACTERISTICS OF THE LATERAL CONTROLLERS WITHOUT  
DISTURBANCES AND UNCERTAINTIES

Controller	$e_{y_{rms}}$ (m)	$e_{y_{max}}$ (m)	$e_{\psi_{rms}}$ (rad)	$e_{\psi_{max}}$ (rad)
Stanley-EMRAN	0.0218	0.0462	0.0089	0.0256
Stanley-EMRAN*	0.0274	0.0677	0.0083	0.0267
Stanley	0.0683	0.2031	0.0160	0.0447
EKF-T2FNN [21]	0.0587	0.0685	0.0050	0.0089
ADRC [21]	0.2207	0.5593	0.0178	0.0363
LQT [21]	0.1939	0.4477	0.0194	0.0270

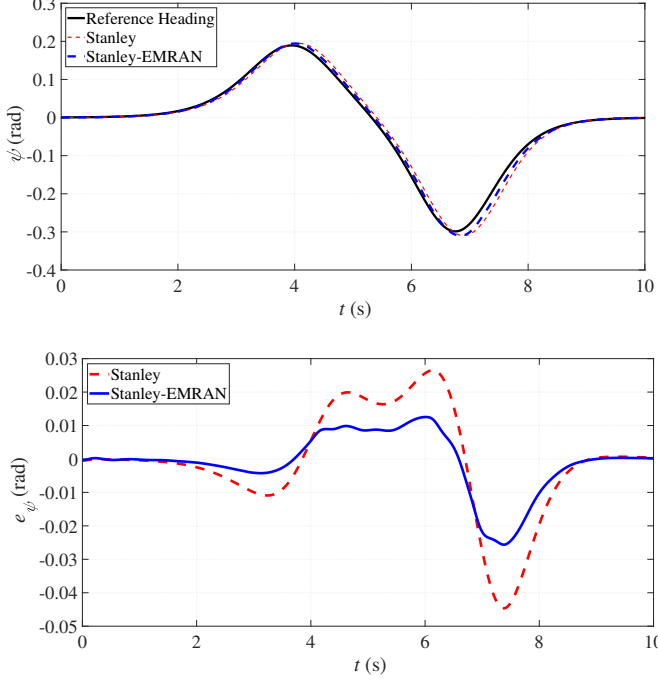


Fig. 10. Vehicle heading and corresponding heading error without external disturbances.

T2FNN) [21]. The Stanley-EMRAN controller outperforms the EKF-T2FNN scheme in terms of minimizing the lateral errors. Though the heading errors with our proposed lateral controller are greater than the EKF-T2FNN, it still has a better tracking ability than the LQT and the previously developed ADRC [18] controller.

Note that the effect of longitudinal dynamics on the path-tracking performance is considered negligible during the simulations with the controllers mentioned above, and thus have limited application in practical scenarios. To address this issue, we use an integrated lateral controller (Stanley-EMRAN\*) coupled with the longitudinal PID-EMRAN for keeping the velocity constant during the DLC maneuvers. From here on, we denote the coupled and decoupled controllers as Stanley-EMRAN\* and Stanley-EMRAN, respectively.

From Table VI, it is seen that the Stanley-EMRAN\* controller is capable of maintaining the desired performance even under the effects of the longitudinal dynamics of the vehicle on the lateral path-tracking control. The results are comparable to Stanley-EMRAN, with minor deviations because of the small variations in the vehicle's velocity during the lane changes.

The yaw rate and the lateral velocity of the vehicle during

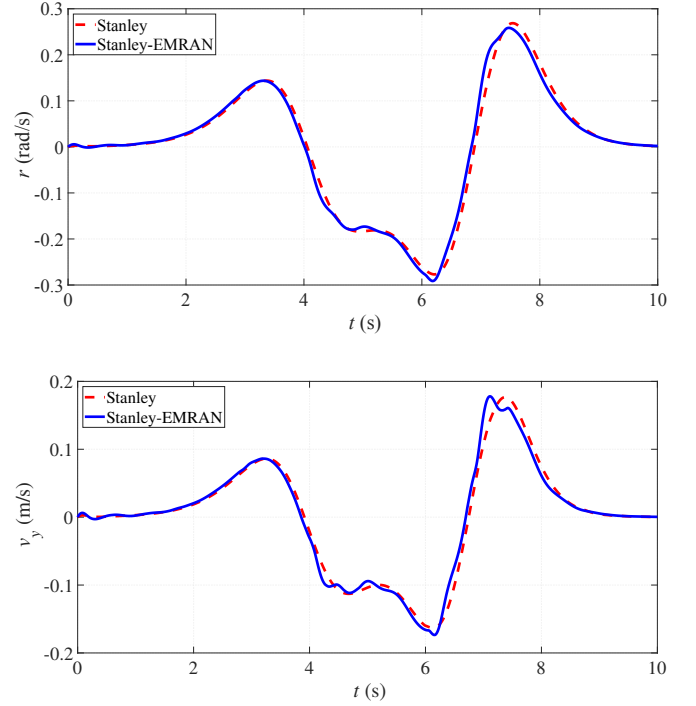


Fig. 11. Yaw rate and lateral velocity for the double lane change maneuver without disturbances and uncertainties.

the DLC maneuver are shown in Fig. 11. Both the Stanley and Stanley-EMRAN controllers maintain the yaw rate and the lateral velocity within a reasonable range, thereby not degrading the stability of the AV.

Figure 12 shows the control input, *i.e.* the steering angle ( $\delta_f$ ) of the proposed controller and the Stanley controller. The figure indicates that the vehicle is able to follow the reference signals accurately without drastic measures from the Stanley-EMRAN controller. The number of hidden neurons added and pruned during the simulation gives an indication of the learning taking place, which is shown in Fig. 13. It may be noted that EMRAN adds neurons when the AV is undergoing the lane changes and prunes when it is in steady-state operation. Neuron peaks are observed during  $7s < t < 9s$  so as to minimize the large lateral and heading errors with the Stanley controller during that time period.

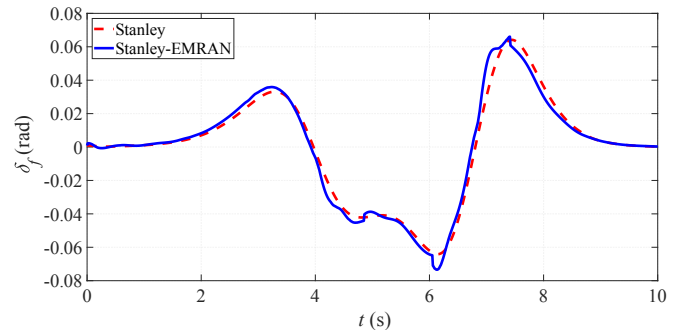


Fig. 12. Steering input for the double lane change maneuver.



TABLE VII  
ERROR CHARACTERISTICS AT SLOW SPEED AND WITH EXTERNAL DISTURBANCE

Controller	$e_{y_{rms}}$ (m)	$e_{y_{max}}$ (m)	$e_{\psi_{rms}}$ (rad)	$e_{\psi_{max}}$ (rad)
Stanley-EMRAN	0.0647	0.0983	0.0145	0.0372
Stanley-EMRAN*	0.0652	0.1188	0.0144	0.0373
Stanley	0.0943	0.2508	0.0197	0.0555

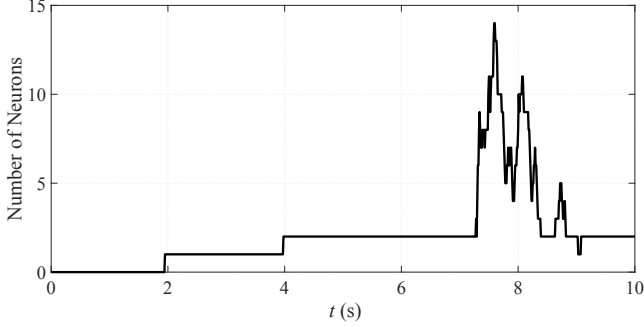


Fig. 13. EMRAN neuron profile during the double lane change maneuver at slow speed and without disturbances.

2) *Case II: Slow Speed and Disturbance*: It is crucial to study the effects of external factors while designing lateral controllers for AVs as they significantly degrade the path-tracking performance. These disturbances can arise from wind gusts, external forces, and varying road friction.

The effectiveness of the Stanley-EMRAN controller has been verified by applying a constant external lateral force of 1500 N on the vehicle. The tracking errors are shown in Fig. 14. Initially, EMRAN starts by learning to approximate

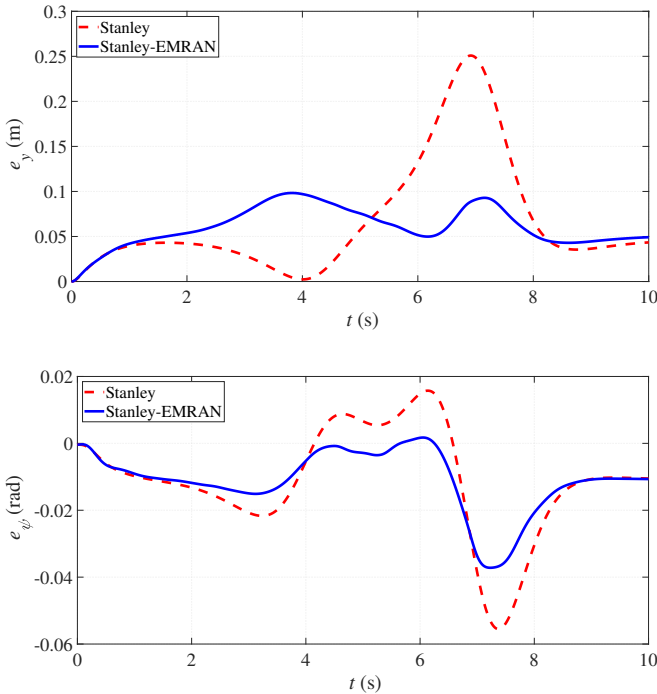


Fig. 14. Tracking errors at slow speed and in presence of a constant external force of 1500 N.

TABLE VIII  
ERROR CHARACTERISTICS AT HIGH SPEED AND WITHOUT DISTURBANCES

Controller	$e_{y_{rms}}$ (m)	$e_{y_{max}}$ (m)	$e_{\psi_{rms}}$ (rad)	$e_{\psi_{max}}$ (rad)
Stanley-EMRAN	0.0913	0.2766	0.0316	0.1277
Stanley-EMRAN*	0.0907	0.2964	0.0312	0.1231
Stanley	0.2163	0.7131	0.0391	0.1558

the nonlinearities due to the disturbance. During this period, the lateral errors ( $e_y$ ) are greater compared to Stanley. It is indicative that once the learning and adaptation process is complete ( $t > 4$  s), the proposed controller significantly reduces both the peaks of lateral and heading errors. Due to the bounded nature of the control input as described in Eq. (2), the steady-state errors cannot be completely eliminated for all the cases. The bounded input to the AV ensures that the vehicle can follow the desired response set as closely as possible without losing its yaw stability. The quantitative results of the controllers are presented in Table VII. The robustness of Stanley-EMRAN to external disturbances is apparent, as it decreases  $e_{y_{max}}$  by 60.8% and  $e_{\psi_{max}}$  by 32.97%. Moreover, the results of the coupled state considering the longitudinal and lateral dynamics suggest that the PID-EMRAN and Stanley-EMRAN\* controllers work coherently in rejecting the effects of the external force. It is also to be noted that the external force is constantly applied throughout the simulation, unlike the investigation in [21]. The neuron history graph is shown in Fig. 15. The controller requires more control effort to mitigate the effect of the disturbance on the AV and, hence, greater number of hidden neurons during the steady-state operation. Furthermore, smaller peaks are observed for this case since EMRAN has already learned the inverse lateral dynamics from the no disturbance test case.

3) *Case III: High Speed and No Disturbance*: Next, we consider the DLC maneuver at a higher constant velocity of 20 m/s, without disturbances. Note that it becomes more difficult for the controllers to control the vehicle when the velocity increases because of the shorter response time. Thus, the tracking errors also increase.

It can be observed from Table VIII and Fig. 16 that the proposed decoupled Stanley-EMRAN controller again provides improved performance compared to that of Stanley by minimizing the overshoots and undershoots, and peak lateral errors.

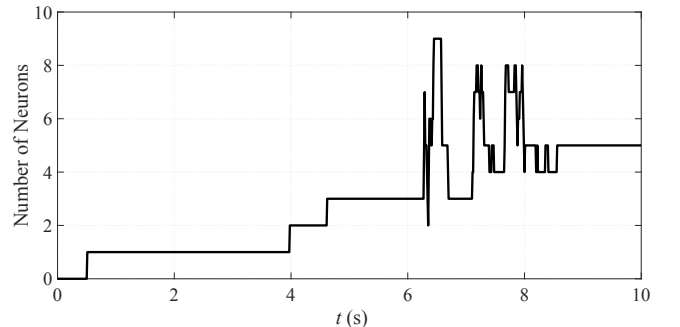


Fig. 15. Neuron history graph of the DLC maneuver at slow speed and with a constant lateral force of 1500 N.

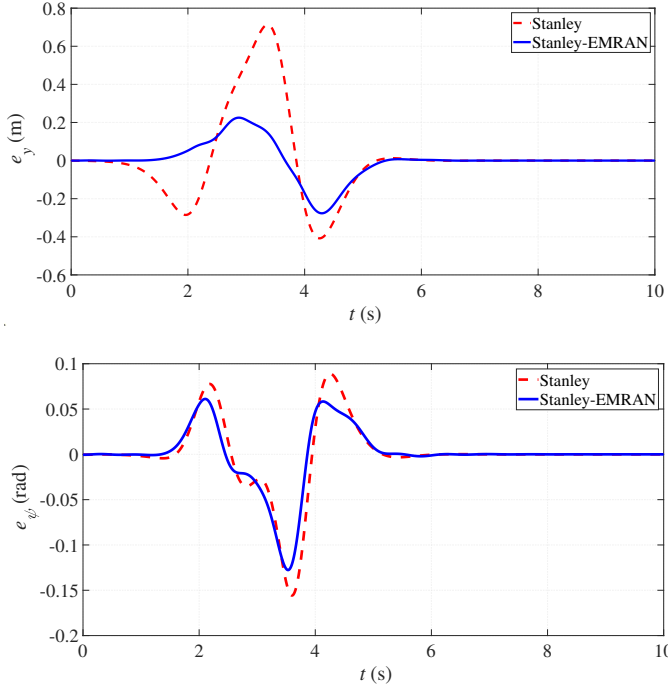


Fig. 16. Tracking errors at high speed and without disturbances.

However, not much improvement is observed in the heading performance since it is not possible to significantly reduce the lateral and heading errors simultaneously with a single control input [20]. In this study, we have focused more on reducing the lateral errors during the path-tracking. Eliminating the lateral error while maintaining the heading error at a reasonable range improves road safety and reduces the possibility of collisions. Additionally, it has been found through simulations that an aggressive heading correction controller degrades the vehicle's stability and passenger comfort.

An increase in  $e_{y_{max}}$  is observed with Stanley-EMRAN\*, a trend observable in all the coupled test cases because of the varying longitudinal dynamics of the vehicle.

4) *Case IV: Parametric Uncertainties:* Finally, uncertainties in tire cornering stiffness ( $C_f$  and  $C_r$ ) and load ( $m$  and  $I_z$ ) are considered at a constant speed of 10 m/s. Table IX presents the minimum and maximum values of these parameters.

The RMS and maximum tracking errors with the parametric uncertainties are calculated in Table X. Both the coupled and decoupled neuro-controllers exhibit the capacity to withstand the perturbations of the internal vehicle parameters when compared to that of Stanley.

Based on the above results of the various test cases, it is evident that the EMRAN based controller scheme can

TABLE IX  
RANGE OF INTERNAL VEHICLE PARAMETERS

Nominal value	Minimum Value	Maximum Value
$m$	$0.8m$	$1.2m$
$I_z$	$0.8I_z$	$1.2I_z$
$C_f$	$0.85C_f$	$1.15C_f$
$C_r$	$0.85C_r$	$1.15C_r$

TABLE X  
RMS AND MAXIMUM TRACKING ERRORS WITH PARAMETRIC UNCERTAINTIES

Controller	$e_{y_{rms}}$ (m)	$e_{y_{max}}$ (m)	$e_{\psi_{rms}}$ (rad)	$e_{\psi_{max}}$ (rad)
Stanley-EMRAN	0.0223	0.0554	0.0089	0.0263
Stanley-EMRAN*	0.0272	0.0598	0.0085	0.0290
Stanley	0.0750	0.2199	0.0166	0.0461

significantly improve the cruise control and path-tracking capabilities of an AV, even under harsh and extreme conditions. It should also be noted that the proposed EMRAN-aided inverse dynamics learning approach can act as an add-on to any other classical feedback controller in achieving a more reliable and accurate tracking response.

## V. CONCLUSIONS

In this paper, an inverse dynamics learning controller based on a feedback error learning mechanism is presented for improving an autonomous vehicle's control under large disturbances and uncertainties. A sequential Radial Basis Function (RBF) neural network called the Extended Minimal Resource Allocating Network (EMRAN) was employed as an aid to the conventional PID and Stanley controllers. Firstly, the effectiveness of the proposed scheme was presented and verified for longitudinal cruise control. Secondly, lateral path-tracking for a Double Lane Change maneuver was investigated for various test cases. We also analyzed the effect of the longitudinal dynamics on the performance of the lateral controller. Performances of the proposed controllers were assessed in terms of the RMS and maximum errors. The results confirm the significant enhancements in tracking performance and show the ability of the EMRAN controller to reconfigure itself under various scenarios.

## ACKNOWLEDGMENT

The authors would like to thank Dr. Dattatray Parle for his valuable suggestions and comments, and would also like to acknowledge the Wipro-IISc Research Innovation Network (WIRIN) for their financial support.

## REFERENCES

- [1] W. Schwarting, J. Alonso-Mora, and D. Rus, "Planning and decision-making for autonomous vehicles," *Annual Review of Control, Robotics, and Autonomous Systems*, vol. 1, no. 1, pp. 187–210, 2018. [Online]. Available: <https://doi.org/10.1146/annurev-control-060117-105157>
- [2] A. Khodayari, A. Ghaffari, S. Ameli, and J. Flahatgar, "A historical review on lateral and longitudinal control of autonomous vehicle motions," in *2010 International Conference on Mechanical and Electrical Technology*, 2010, pp. 421–429.
- [3] I. A. Ntousakis, I. K. Nikolos, and M. Papageorgiou, "On microscopic modelling of adaptive cruise control systems," *Transportation Research Procedia*, vol. 6, pp. 111–127, 2015.
- [4] G. Lie, R. Zejian, G. Pingshu, and C. Jing, "Advanced emergency braking controller design for pedestrian protection oriented automotive collision avoidance system," *The Scientific World Journal*, vol. 2014, 2014.
- [5] S. Xu, H. Peng, Z. Song, K. Chen, and Y. Tang, "Accurate and smooth speed control for an autonomous vehicle," in *2018 IEEE Intelligent Vehicles Symposium (IV)*, 2018, pp. 1976–1982.

- [6] J. Ploeg, B. T. M. Scheepers, E. van Nunen, N. van de Wouw, and H. Nijmeijer, "Design and experimental evaluation of cooperative adaptive cruise control," in *2011 14th International IEEE Conference on Intelligent Transportation Systems (ITSC)*, 2011, pp. 260–265.
- [7] V. Milanés, S. E. Shladover, J. Spring, C. Nowakowski, H. Kawazoe, and M. Nakamura, "Cooperative adaptive cruise control in real traffic situations," *IEEE Transactions on Intelligent Transportation Systems*, vol. 15, no. 1, pp. 296–305, 2014.
- [8] Z. Wang, G. Wu, and M. J. Barth, "A review on cooperative adaptive cruise control (cacc) systems: Architectures, controls, and applications," in *2018 21st International Conference on Intelligent Transportation Systems (ITSC)*, 2018, pp. 2884–2891.
- [9] S. Lefevre, A. Carvalho, and F. Borrelli, "Autonomous car following: A learning-based approach," in *2015 IEEE Intelligent Vehicles Symposium (IV)*, 2015, pp. 920–926.
- [10] S. Wang, Y. Hui, X. Sun, and D. Shi, "Neural network sliding mode control of intelligent vehicle longitudinal dynamics," *IEEE Access*, vol. 7, pp. 162 333–162 342, 2019.
- [11] Z. Huang, X. Xu, H. He, J. Tan, and Z. Sun, "Parameterized batch reinforcement learning for longitudinal control of autonomous land vehicles," *IEEE Transactions on Systems, Man, and Cybernetics: Systems*, vol. 49, no. 4, pp. 730–741, 2019.
- [12] J. Pérez, A. Gajate, V. Milanés, E. Onieva, and M. Santos, "Design and implementation of a neuro-fuzzy system for longitudinal control of autonomous vehicles," in *International Conference on Fuzzy Systems*, 2010, pp. 1–6.
- [13] M. Buechel and A. Knoll, "Deep reinforcement learning for predictive longitudinal control of automated vehicles," in *2018 21st International Conference on Intelligent Transportation Systems (ITSC)*, 2018, pp. 2391–2397.
- [14] L. Nie, J. Guan, C. Lu, H. Zheng, and Z. Yin, "Longitudinal speed control of autonomous vehicle based on a self-adaptive pid of radial basis function neural network," *IET Intelligent Transport Systems*, vol. 12, no. 6, pp. 485–494, 2018.
- [15] S. Kumarawadu and T. T. Lee, "Neuroadaptive combined lateral and longitudinal control of highway vehicles using rbf networks," *IEEE Transactions on Intelligent Transportation Systems*, vol. 7, no. 4, pp. 500–512, 2006.
- [16] J. Jiang and A. Astolfi, "Lateral control of an autonomous vehicle," *IEEE Transactions on Intelligent Vehicles*, vol. 3, no. 2, pp. 228–237, 2018.
- [17] X. Yuan, G. Huang, and K. Shi, "Improved adaptive path following control system for autonomous vehicle in different velocities," *IEEE Transactions on Intelligent Transportation Systems*, vol. 21, no. 8, pp. 3247–3256, 2020.
- [18] Y. Xia, F. Pu, S. Li, and Y. Gao, "Lateral path tracking control of autonomous land vehicle based on adrc and differential flatness," *IEEE Transactions on Industrial Electronics*, vol. 63, no. 5, pp. 3091–3099, 2016.
- [19] P. Petrov and F. Nashashibi, "Modeling and nonlinear adaptive control for autonomous vehicle overtaking," *IEEE Transactions on Intelligent Transportation Systems*, vol. 15, no. 4, pp. 1643–1656, 2014.
- [20] X. Ji, X. He, C. Lv, Y. Liu, and J. Wu, "Adaptive-neural-network-based robust lateral motion control for autonomous vehicle at driving limits," *Control Engineering Practice*, vol. 76, pp. 41–53, 2018. [Online]. Available: <https://www.sciencedirect.com/science/article/pii/S0967066118300881>
- [21] H. Taghavifar, C. Hu, Y. Qin, and C. Wei, "EKF-neural network observer based type-2 fuzzy control of autonomous vehicles," *IEEE Transactions on Intelligent Transportation Systems*, pp. 1–13, 2020.
- [22] G. Han, W. Fu, W. Wang, and Z. Wu, "The lateral tracking control for the intelligent vehicle based on adaptive pid neural network," *Sensors*, vol. 17, no. 6, p. 1244, 2017.
- [23] X. Huang, H. Zhang, G. Zhang, and J. Wang, "Robust weighted gain-scheduling  $H_\infty$  vehicle lateral motion control with considerations of steering system backlash-type hysteresis," *IEEE Transactions on Control Systems Technology*, vol. 22, no. 5, pp. 1740–1753, 2014.
- [24] C. Latrach, M. Kchaou, A. El Hajjaji, and A. Rabhi, "Robust  $H_\infty$  fuzzy networked control for vehicle lateral dynamics," in *16th International IEEE Conference on Intelligent Transportation Systems (ITSC 2013)*, 2013, pp. 905–910.
- [25] C. Piao, X. Liu, and C. Lu, "Lateral control using parameter self-tuning lqr on autonomous vehicle," in *2019 International Conference on Intelligent Computing, Automation and Systems (ICICAS)*. IEEE, 2019, pp. 913–917.
- [26] S.-H. Lee and C. C. Chung, "Predictive control with sliding mode for autonomous driving vehicle lateral maneuvering," in *2017 American Control Conference (ACC)*. IEEE, 2017, pp. 2998–3003.
- [27] A. Norouzi, M. Masoumi, A. Barari, and S. Farokhpour Sani, "Lateral control of an autonomous vehicle using integrated backstepping and sliding mode controller," *Proceedings of the Institution of Mechanical Engineers, Part K: Journal of Multi-body Dynamics*, vol. 233, no. 1, pp. 141–151, 2019.
- [28] S. Krishna, S. Narayanan, and S. D. Ashok, "Fuzzy logic based yaw stability control for active front steering of a vehicle," *Journal of Mechanical Science and Technology*, vol. 28, no. 12, pp. 5169–5174, 2014.
- [29] S. Di Cairano, H. E. Tseng, D. Bernardini, and A. Bemporad, "Vehicle yaw stability control by coordinated active front steering and differential braking in the tire sideslip angles domain," *IEEE Transactions on Control Systems Technology*, vol. 21, no. 4, pp. 1236–1248, 2013.
- [30] S. Li, G. Wang, B. Zhang, Z. Yu, and G. Cui, "Vehicle yaw stability control at the handling limits based on model predictive control," *International Journal of Automotive Technology*, vol. 21, no. 2, pp. 361–370, 2020.
- [31] W. Huang, P. K. Wong, K. I. Wong, C. M. Vong, and J. Zhao, "Adaptive neural control of vehicle yaw stability with active front steering using an improved random projection neural network," *Vehicle System Dynamics*, vol. 59, no. 3, pp. 396–414, 2021.
- [32] J. R. Noriega and H. Wang, "A direct adaptive neural-network control for unknown nonlinear systems and its application," *IEEE transactions on neural networks*, vol. 9, no. 1, pp. 27–34, 1998.
- [33] H. Wang, P. X. Liu, S. Li, and D. Wang, "Adaptive neural output-feedback control for a class of nonlinear triangular nonlinear systems with unmodeled dynamics," *IEEE transactions on neural networks and learning systems*, vol. 29, no. 8, pp. 3658–3668, 2017.
- [34] A. Pashilkar, N. Sundararajan, and P. Saratchandran, "A fault-tolerant neural aided controller for aircraft auto-landing," *Aerospace Science and Technology*, vol. 10, no. 1, pp. 49–61, 2006.
- [35] S. Suresh, S. Narasimhan, S. Nagarajaiah, and N. Sundararajan, "Fault-tolerant adaptive control of nonlinear base-isolated buildings using emran," *Engineering Structures*, vol. 32, no. 8, pp. 2477–2487, 2010.
- [36] S. Narasimhan, S. Suresh, and N. Sundararajan, "Direct adaptive neural controller for earthquake excited nonlinear base isolated buildings," in *2007 IEEE 22nd International Symposium on Intelligent Control*. IEEE, 2007, pp. 138–143.
- [37] F. J. Darsivan, W. F. Faris, and W. Martono, "Active engine mounting controller using extended minimal resource allocating networks," *International Journal of Vehicle Noise and Vibration*, vol. 4, no. 2, pp. 150–168, 2008.
- [38] Y. Li, N. Sundararajan, and P. Saratchandran, "Analysis of minimal radial basis function network algorithm for real-time identification of nonlinear dynamic systems," *IEE Proceedings-Control Theory and Applications*, vol. 147, no. 4, pp. 476–484, 2000.
- [39] M. Graf Plessen, D. Bernardini, H. Esen, and A. Bemporad, "Spatial-based predictive control and geometric corridor planning for adaptive cruise control coupled with obstacle avoidance," *IEEE Transactions on Control Systems Technology*, vol. 26, no. 1, pp. 38–50, 2018.
- [40] R. Rajamani, *Vehicle dynamics and control*. Springer Science & Business Media, 2011.
- [41] M. K. Salaani, "Analytical tire forces and moments model with validated data," *SAE Transactions*, pp. 735–763, 2007.
- [42] K. Liu, J. Gong, A. Kurt, H. Chen, and U. Ozguner, "Dynamic modeling and control of high-speed automated vehicles for lane change maneuver," *IEEE Transactions on Intelligent Vehicles*, vol. 3, no. 3, pp. 329–339, 2018.
- [43] T. Suzuki and H. Fujimoto, "Slip ratio estimation and regenerative brake control without detection of vehicle velocity and acceleration for electric vehicle at urgent brake-turning," in *2010 11th IEEE International Workshop on Advanced Motion Control (AMC)*, 2010, pp. 273–278.
- [44] J. Platt, "A resource-allocating network for function interpolation," *Neural computation*, vol. 3, no. 2, pp. 213–225, 1991.
- [45] H. Gomi and M. Kawato, "Learning control for a closed loop system using feedback-error-learning," in *29th IEEE Conference on Decision and Control*, 1990, pp. 3289–3294 vol.6.
- [46] G. M. Hoffmann, C. J. Tomlin, M. Montemerlo, and S. Thrun, "Autonomous automobile trajectory tracking for off-road driving: Controller design, experimental validation and racing," in *2007 American Control Conference*, 2007, pp. 2296–2301.
- [47] B. Paden, M. Čáp, S. Z. Yong, D. Yershov, and E. Frazzoli, "A survey of motion planning and control techniques for self-driving urban vehicles," *IEEE Transactions on Intelligent Vehicles*, vol. 1, no. 1, pp. 33–55, 2016.

- [48] N. H. Amer, K. Hudha, H. Zamzuri, V. R. Aparow, Z. A. Kadir, and A. F. Z. Abidin, "Hardware-in-the-loop simulation of trajectory following control for a light armoured vehicle optimised with particle swarm optimisation," *International Journal of Heavy Vehicle Systems*, vol. 26, no. 5, pp. 663–691, 2019.
- [49] C. R. Houck, J. Joines, and M. G. Kay, "A genetic algorithm for function optimization: a matlab implementation," *Ncsu-ie tr*, vol. 95, no. 09, pp. 1–10, 1995.